Article

Raman Spectroscopy of Two-Dimensional Bi$_2$Te$_x$Se$_{3-x}$ Platelets Produced by Solvothermal Method

Jian Yuan [1], Meng Zhao [2], Wengzhi Yu [1], Yao Lu [1], Caiyun Chen [1], Meng Xu [1], Shaojuan Li [1], Kian Ping Loh [2] and QiaoliangBao [1,3,*]

[1] Institute of Functional Nano and Soft Materials (FUNSOM), Jiangsu Key Laboratory for Carbon-Based Functional Materials and Devices, and Collaborative Innovation Center of Suzhou Nano Science and Technology, Soochow University, Suzhou 215123, China;
E-Mails: 20124214040@suda.edu.cn (J.Y.); 20144214003@stu.suda.edu.cn (W.Y.);
20134214095@stu.suda.edu.cn (Y.L.); 20124214017@suda.edu.cn (C.C.);
xujane1225@gmail.com (M.X.); sjli@suda.edu.cn (S.L.)

[2] Department of Chemistry, and Graphene Research Centre, National University of Singapore, 3 Science Drive 3, Singapore 117543, Singapore; E-Mails: zhaomeng@nus.edu.sg (M.Z.); chmlohkp@nus.edu.sg (K.P.L.)

[3] Department of Materials Science and Engineering, Monash University, Clayton, VIC 3800, Australia

* Author to whom correspondence should be addressed; E-Mail: qlbao@suda.edu.cn;
Tel.: +86-512-6588-0722; Fax: +86-512-6588-2846.

Academic Editor: Jordi Sort

Abstract: In this paper, we report a facile solvothermal method to produce both binary and ternary compounds of bismuth chalcogenides in the form of Bi$_2$Te$_x$Se$_{3-x}$. The crystal morphology in terms of geometry and thickness as well as the stoichiometric ratio can be well controlled, which offers the opportunities to systematically investigate the relationship between microstructure and phonon scattering by Raman spectroscopy. Raman spectra of four compounds, *i.e.*, Bi$_2$Se$_3$, Bi$_2$Se$_2$Te, Bi$_2$SeTe$_2$ and Bi$_2$Te$_3$, were collected at four different excitation photon energies (2.54, 2.41, 1.96, and 1.58 eV). It is found that the vibrational modes are shifted to higher frequency with more Se incorporation towards the replacement of Te. The dependence of Raman vibrational modes on excitation photon energy was investigated. As the excitation photon energy increases, three Raman vibrational modes (A_{1g}^1, E_g^2 and A_{1g}^2) of the as-produced compounds move to low frequency. Three Infrared-active (IR-active) modes were observed in thin topological insulators (TIs) crystals.

1. Introduction

Topological insulators (TIs) such as bismuth telluride, antimony telluride and other binary/ternary group V−VI compounds, are emerging electronic materials that have a bulk band gap similar to conventional insulator but possessing protected conducting states on their edge or surface [1–3]. Owing to the emerging theoretical prediction of transport without dissipation in two-dimensional (2D) TIs, diverse experimental works about the quantum-spin Hall effects have been reported [4–6]. The exotic physical properties of 2D TIs have stimulated extensive range of applications for electronic [7], optoelectronic [8], and thermoelectric devices [9]. The fast progress in the area demands large scale production of high-quality 2D TI crystals with desired structure and properties. However, it is still challenging to control the crystal morphology perfectly in terms of geometry and thickness as well as the stoichiometric ratio [3,10]. Furthermore, the light-matter interactions in 2D TIs with respect to phonon scattering and the dependence of these interactions on the microstructure are not well understood [11].

In this work, we present a facile solvothermal method to synthesize $Bi_2Te_xSe_{3-x}$ platelets in large scale and with high yield [12–16]. The use of ethylene glycol (EG) as both reducing agent and solvent makes the synthesis process simple and friendly [17]. The systematic material characterizations on four products (Bi_2Se_3, Bi_2Se_2Te, Bi_2SeTe_2 and Bi_2Te_3) indicate the successful growth of TI platelets with controlled morphology and high quality. The systematic Raman spectroscopy characterizations reveal that the characteristic peaks are dependent on the photon energy as well as the elemental composition and new vibration modes can be observed with lower photon energy.

2. Experimental

2.1. Material Synthesis

Bismuth nitrate ($Bi(NO_3)_3$), bismuth oxide (Bi_2O_3), seleniumoxide (SeO_2) and tellurium oxide (TeO_2) were purchased from Alfa Aesar. Polyvinylpyrrolidone (PVP, K30) were purchased from TCI, Sodium hydroxide (NaOH) and ethylene glycol (EG) was acquired from Shanghai Chemical Reagent Co. (Shanghai, China) All the chemicals used for the synthesis of $Bi_2Te_xSe_{3-x}$ sheets in the present work are of analytical grade without further purification.

For the synthesis of Bi_2Te_3, 0.5 mmol $Bi(NO_3)_3$, 0.75 mmol TeO_2, 2 mL NaOH (8 mol/L) and 0.4 g PVP were mixed and dissolved in 18 mL EG, followed by stirring for 1 h and the mixture was then transferred into a stainless steel autoclave with Teflon lining up to 40%–60% of the capacity. The autoclave was heated at 200 °C in an oven for 24 h and then cooled down to room temperature. The residual gray powders were washed with deionized water and ethanol and finally dried at 60 °C in a vacuum chamber overnight. The other three compounds (Bi_2Te_2Se, Bi_2TeSe_2 and Bi_2Se_3) were also synthesized by the similar procedure as described above. The differences from the previous growth are the change in their reaction temperature as 220 °C and the concentrations of NaOH are maintained at 4, 1 and 0.5 mol/L, respectively.

2.2. Material Characterizations

The phase structure of the final products was investigated by X-ray diffractometer (XRD, PANAlytical, EMPYREAN, Almelo, The Netherlands) using Cu Kα radiation ($\lambda = 1.541$ Å). Scanning electron microscopy (SEM, FEI Quanta 200 FEG, FEI, Hillsboro, OR, USA) was employed to study the morphology of the products. The microstructure was examined with the aid of high-resolution transmission electron microscopy (HRTEM, FEI Tecnai G2 F20 STWIN, FEI). Raman spectra of nanostructured $Bi_2Te_xSe_{3-x}$ samples were recorded using confocal Raman spectrometer (Horiba Jobin Yvon, Labram HR 800, Horiba Jobin Yvon, Paris, France) with four different excitation photon energy (2.54 eV (488 nm), 2.41 eV (514 nm), 1.96 eV (633 nm), and 1.58 eV (785 nm)) at room temperature. The laser power is fixed to be $\sim 4 \times 10^5$ W/cm^{-2} at different wavelengths. The measured spectral range is 10–200 cm^{-1} and the spectral resolution is 0.5 cm^{-1} using the 1800 groove/mm grating. The topography and thickness of the as-produced samples were determined by atomic force microscope (AFM, Bruker, Veeco Multimode V, Bruker, Santa Barbara, CA, USA).
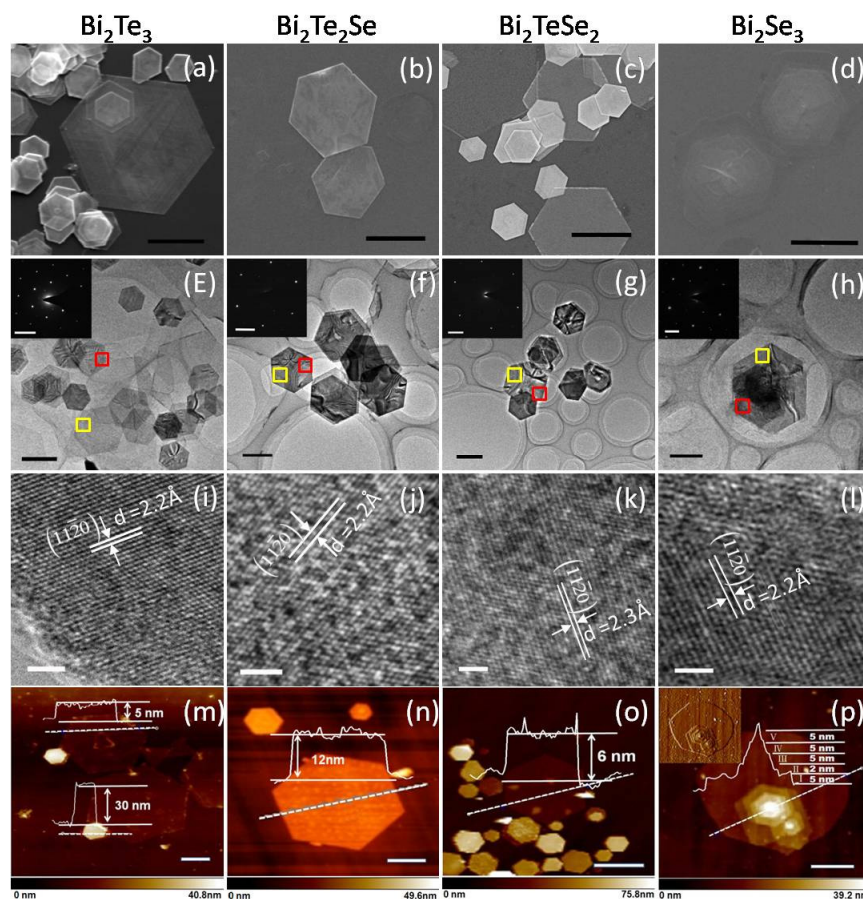
3. Results and Discussion

The material growth parameters are very critical in the synthesis of both binary and ternary $A_2^VB_3^{VI}$-type hexagonal platelets via solvothermal method. It is generally believed that the reaction time, reaction temperature, the concentration of alkalis and the surfactants (PVP) are key factors that affect the crystallization of $Bi_2Te_xSe_{3-x}$ [14]. The formation of $Bi_2Te_xSe_{3-x}$ platelets includes two major steps: (i) reduction of Bi_2O_3 and TeO_2/SeO_2 by EG; and (ii) oriented attachment of the Bi-Te/Bi-Se alloy particles into crystalline platelets with hexagonal shape [13]. We have found that NaOH plays a vital role in the reduction process regarding step (i) and PVP serve as a template for the crystal growth in step (ii), which is discussed in detail elsewhere [18].

Figure 1 shows the materials characterization data of the as-produced four compounds, *i.e.*, Bi_2Se_3, Bi_2Se_2Te, Bi_2SeTe_2 and Bi_2Te_3. Figure 1a depicts the typical SEM image of Bi_2Te_3 platelets. It is clearly seen that the high-yield hexagonal nanosheets were obtained with the size ranging from 400 nm to 5 μm. The regular shape and sharp edges indicate excellent crystallinity. Figure 1e shows the typical TEM image of Bi_2Te_3 platelets, in which the relative uniform contrast demonstrates a small difference in thickness. The selected area electron diffraction (SAED) pattern shown in the inset of Figure 1e can be indexed to the [001] zone axis of rhombohedral Bi_2Te_3, indicating that the nanosheet is single crystal with a preferential (001) orientation. As the top-bottom facets are indexed to be {0001} while the six edge facets are {11$\bar{2}$0}, the growth of the hexagon platelet is determined to be along ⟨11$\bar{2}$0⟩ direction, which is consistent with the previous report. The HRTEM image in Figure 1i clearly shows that the lattice fringes are structurally uniform with a spacing of 2.2 Å and is in good agreement with that of the (110) planes of rhombohedral phase. The representative AFM topography is shown in Figure 1m where the Bi_2Te_3 platelet has a flat surface with thickness of 12 nm.

Figure 1b,c shows the SEM morphologies of ternary V-VI based alloys Bi_2Te_2Se and Bi_2TeSe_2, in which hexagonal platelets are observed. The microstructure of these two compounds shown in Figure 1f,g confirms the nature of single crystal with rhombohedral symmetry. The size of the platelets is in the average of about 500 nm to a few micrometers. The HRTEM images in Figure 1j,k clearly reveal the

lattice of {11$\bar{2}$0} facet with spacing of 2.2 Å and 2.3 Å, respectively. It was examined that the ternary platelets are well-crystallized with less atomic defects, which are similar to those of Bi_2Te_3 platelets. The AFM images shown in Figure 1n,o indicate that the platelets have a thickness in the range of 6 to 25 nm.

Figure 1d,h show representative SEM and TEM images of Bi_2Se_3 platelets. It is interesting to see that these hexagonal crystals are stacking together, indicating that these platelets nucleate from the same seed. The SAED result taken from bilayer region (red square in the inset of Figure 1h) presents only one set of hexagonal pattern, suggesting that these two layers are of the same crystal orientation. The SAED pattern can be indexed to be [001] zone axis of the rhombohedral Bi_2Se_3. The multilayer stacking can be further confirmed by AFM topography and phase images, as shown in Figure 1p and its inset. The height profile (Figure 1p) displays obvious plateaus with step height of about 5 nm. The HRTEM image in Figure 1l clearly presents the lattice fringes, which are structurally uniform with spacing of 2.2 Å, and is in good agreement with the previous report [19].

Figure 1. Characterizations of Bi_2Te_3, Bi_2Te_2Se, Bi_2TeSe_2 and Bi_2Se_3 platelets. (**a**–**d**) Scanning electron microscopy (SEM) and (**e**–**h**) transmission electron microscopy (TEM) images of these four compounds. The insets of (**e**–**h**) are selected area electron diffraction (SAED) patterns taken at the red square area in the TEM image. Scale bars in (**a**–**d**) are 1 μm. Scale bars in (**e**–**h**) are 500 nm. (**i**–**l**) High-resolution transmission electron microscopy (HRTEM) images taken at the yellow square area in TEM images (**e**–**h**). Scale bars: 2 nm. (**m**–**p**) Typical atomic force microscope (AFM) images and height profiles of Bi_2Te_3, Bi_2Te_2Se, Bi_2TeSe_2 and Bi_2Se_3 platelets. The height profiles floating on the images were taken at the dashed lines. The inset in (**p**) shows the phase image. Scale bars: 1 μm.

The crystal structure and phase of the as-prepared samples were verified by XRD, as shown in Figure 2. Three strongest peaks in each spectrum can be fully indexed to the reflections of three facets (*i.e.*, (003), (006) and (0015)) in rhombohedral phase. On the basis of XRD pattern, Bi_2Se_3, possessing a preferred growth direction of (006), is assigned to have rhombohedral phase with lattice constants a = 4.140 Å, c = 28.636 Å (refer to JCPDS Card Number 82-0358) [13], space group: $R\overline{3}m$ (D_{3d}^5). The lattice constants of Bi_2TeSe_2 is found to be relatively close to that of Bi_2Se_3, *i.e.*, a = 4.218 Å, c = 29.240 Å. By contrast, the lattice parameters of the other two compounds (Bi_2SeTe_2 and Bi_2Te_3) are slightly larger, a = 4.303 Å, c = 30.010 Å for Bi_2SeTe_2 and a = 4.390 Å, c = 30.460 Å for Bi_2Te_3. This suggests that the unit cells of Bi_2SeTe_2 and Bi_2Te_3 are expanded along the in-plane and out-of-plane directions (*i.e.*, along both a and c directions) due to the bonding with larger atom Te.

In order to determine the vibrational modes, it is important to investigate the atomic structure and chemical bonds of this group of compounds. According to XRD results, all four compounds are assigned to be layered rhombohedral crystal with space group $R\overline{3}m$ (D_{3d}^5), which is schematically shown in Figure 3a. These materials consist of anisotropic layers in which five mono-atomic planes are covalently bonded to form a quintuple layer. These quintuple layers are weakly bound to each other by the van der Waals forces and can be described as following: $-A_{VI}^{(1)}-B_V-A_{VI}^{(2)}-B_V-A_{VI}^{(1)}-$, where A_{VI} refers to either Te or Se, and B_V stands for Bi. The superscripts on the A atoms designate the different positions within the five-fold layers and the five-layer stacks are centro-symmetrical with respect to $A_{VI}^{(2)}$, which plays the role of an inversion center [20]. As the primitive unit cell contains five atoms according to the chemical formula, it means that there are 15 lattice vibrational modes. Consequently, there are 15 lattice dynamical modes locate at the Brillouin zone center (q = 0), including three acoustic modes and 12 optical modes. Therefore, group theory allows Γ_{bulk}-center modes, which decompose in the irreducible representations and can be described as $\Gamma_{bulk} = 2A_{1g} + 3A_{2u} + 2E_g + 3E_u$ [21,22]. These phonon modes are exclusively either Raman or infrared (IR) active [23,24] due to the inversion crystal symmetry. Specifically, the A_{1g} and E_g modes are Raman active, while the A_{2u} and E_u modes of non-zero frequency are IR-active, as illustrated in Figure 3b.

As the A_{1g} mode is attributed to the symmetric out-of-plane stretching of A_{VI}-B_V atoms vibrating in opposite directions, a short displacement induces higher phonon frequency. Whereas E_g mode is caused by symmetric in-plane bending and shearing the upper two layers of A_{VI}-B_V atoms vibrating in the same direction, which make a greater atomic displacement by producing lower phonon frequency. Since the A_g modes are vibrating out of phase, the bonding of each neighboring atom is stronger than that of the E_g modes. As a result, the atomic vibration displacement of A_g modes is restricted and the atomic vibrational frequency of A_g modes is stronger than that of E_g modes, which is experimentally verified here in after.
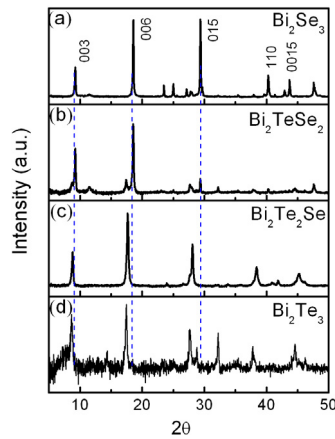
Figure 4 depicts the Raman spectra of all the four samples measured with four different excitation photon energies (2.54, 2.41, 1.96, and 1.58 eV). We can observe three main peaks in the Raman spectra of these four compounds corresponding to A_{1g}^1, E_g^2 and A_{1g}^2, respectively. It is found that stronger resonant peaks especially A_{1g}^1 can be observed with lower excitation photon energy, which may be correlated to the resonant condition and larger skin depth at longer wavelengths. For the Te rich compounds (Bi_2SeTe_2 and Bi_2Te_3), the stretching modes of A_{1g}^1 and A_{1g}^2 appear at 62 cm^{-1} and 137 cm^{-1}, respectively. The A_{1g}^2 mode is significantly red-shift compared with that measured at low temperature (*i.e.*, 8 K). [25] The bending mode of E_g^2 is found at 102 cm^{-1}. For the Se rich compounds (Bi_2TeSe_2 and

Bi_2Se_3), all the three Raman peaks are shifted to higher frequency, *i.e.*, the stretching modes of A_{1g}^1 and A_{1g}^2 appearing at ~72 cm^{-1} and ~172 cm^{-1}, respectively, along with the bending mode of E_g^2 at ~130 cm^{-1}.
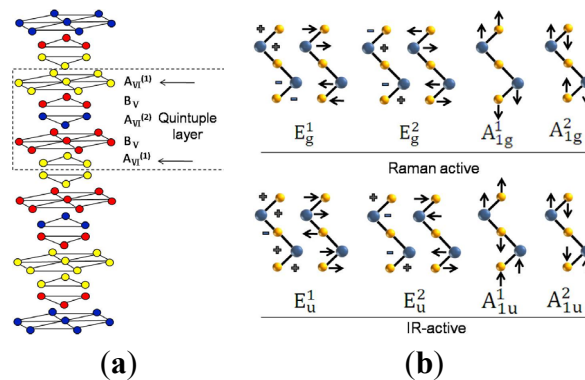
We further investigate the dependence of frequency of vibrational modes on the photon energy for all four compounds, as shown in Figure 5. The peak positions show weak dependence on the photon energy in terms of small frequency shift, which may be due to the fact that our samples have more than five quintuple layers. However, we can still observe the general trend that these three Raman vibrational modes (especially A_{1g}^2 and E_g^2) of the as-produced four compounds shift to higher frequencies while the excitation photon energy varies from 2.54 to 1.58 eV. The frequency dependence observed here is correlated to non-uniform phonon dispersion of these modes throughout the Brillouin zones [26,27]. For example, the A_g^1 mode corresponds to the longitudinal phonon vibration, which leads to a resonance on the Γ–Z direction with the increasing of excitation photon energy. As revealed by the phonon dispersion diagrams, [23,26] A_g^1 modes of $Bi_2Te_xSe_{3-x}$ become soft along the Γ–Z direction, resulting in the shift towards lower frequency at Γ point. This is qualitatively in agreement with our experimental observations. Nevertheless, the heating effect induced by the laser with lower photon energy could be another innegligible factor for the observed Raman peak shift.

In order to further understand the effect of stoichiometric ratio on vibrational modes, we re-plot the Raman spectra excited at 1.58 eV in Figure 6a,b. The frequency shift of all the Raman modes in the $Bi_2Te_xSe_{3-x}$ system is observed for $x \in (0, 1, 2, 3)$, corresponding to the substitution of the Te atoms by Se. It is found that the vibrational modes are shifted to higher frequency with more Se incorporation towards the replacement of Te. This is because of the smaller size of Se atoms with stronger electro-negativity, which leads to the shortening of the chemical bonds between Se and Bi. This observation agrees with the XRD results above-mentioned, which suggest that Se rich compounds have smaller unit cell. It is interesting to observe large peak shift for E_g^2 and A_{1g}^2 modes (>25 cm^{-1}) while the chemical composition is changed from Bi_2Te_2Se to Bi_2TeSe_2. In comparison, the position of A_{1g}^1 mode does not have significant shift for the reason that the out-of-plane stretching is not so sensitive to the change of chemical bonds.
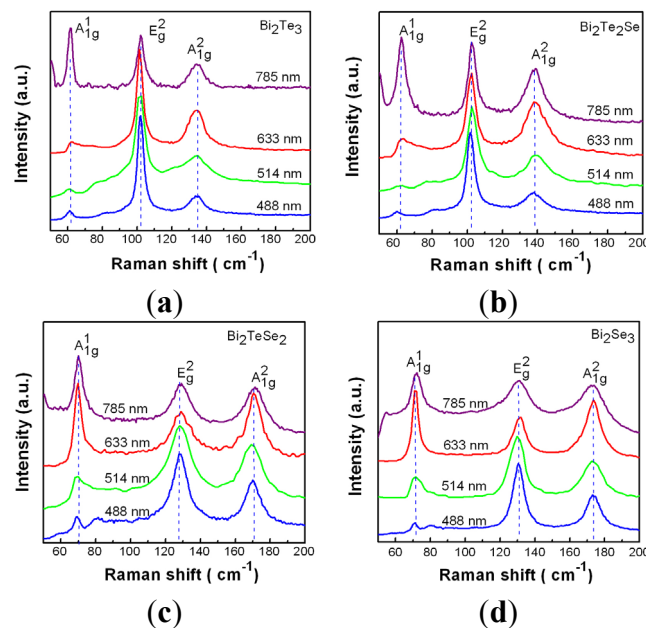
Interestingly, we observed two IR-active modes in some TI crystals, *i.e.*, E_u mode at 110 cm^{-1} for Bi_2Se_3 and A_{2u}^1 at 92 cm^{-1} for Bi_2Te_3, as indicated in Figure 6c [27–29]. It is assumed that the appearance of these modes is caused by the size effect in the nanoplatelets. In case of Bi_2Te_3, the new peak are identified as A_{2u} mode composed of longitudinal optical (LO) phonons at the Brillouin zone boundary (Z point). In principle, the A_{2u} mode is not Raman-active mode but IR-active mode in bulk Bi_2Te_3 crystals. However, this IR-active mode is observable in case of symmetry breaking in which infinite crystal periodicity is absent. For example, the A_{2u}^1 mode at 92 cm^{-1} can be explained by the surface phonon mode, which is only observed in nano-sized materials [30]. In case of Bi_2Se_3, E_u mode at 110 cm^{-1} was experimentally observed for the first time. It has been theoretically predicted that E_u mode is correlated to the in-plane vibration, which is only observable in very thin Bi_2Se_3 sheet. A prominent vibrational mode at 115 cm^{-1} is also observed in Bi_2Te_3, as shown in Figure 6c. According to previous report on bismuth chalcogenide nanoplates [31,32], this new peak of Bi_2Te_3 are likely originated from Te impurities because laser can cause Te-containing compound to decompose and lead to strong Te Raman features.

Figure 2. X-ray diffractometer (XRD) patterns of the as-grown four compounds (Bi_2Te_3, Bi_2Te_2Se, Bi_2TeSe_2 and Bi_2Se_3).
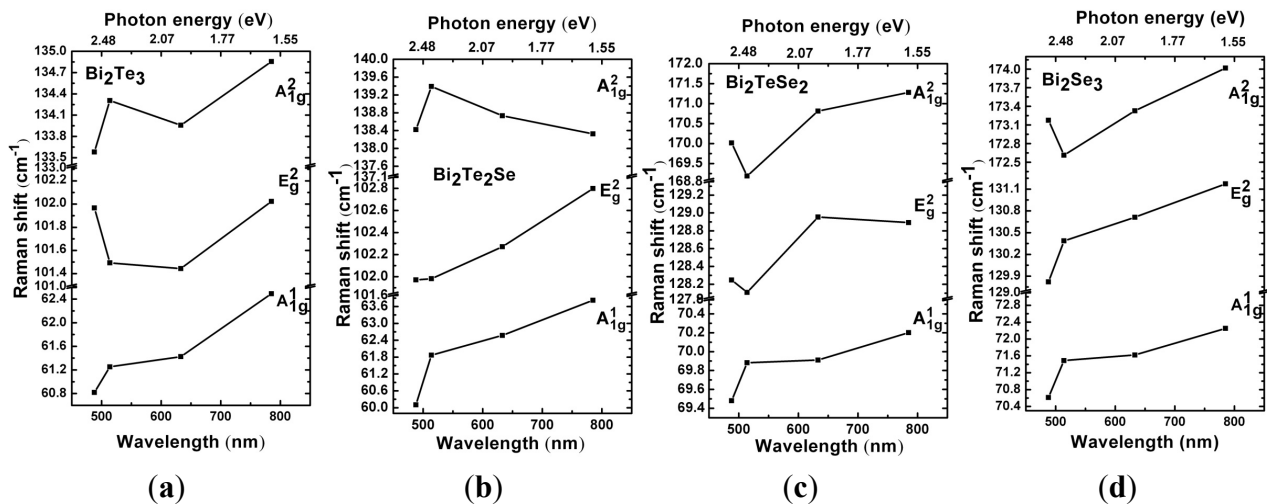

(**a**)　　　　　　　　　(**b**)

Figure 3. (**a**) Schematic diagram of $Bi_2Te_xSe_{3-x}$ crystal structure. (**b**) Schematic diagram of Raman active and Infrared-active (IR-active) vibration modes.

(**a**)　　　　　　　　　(**b**)
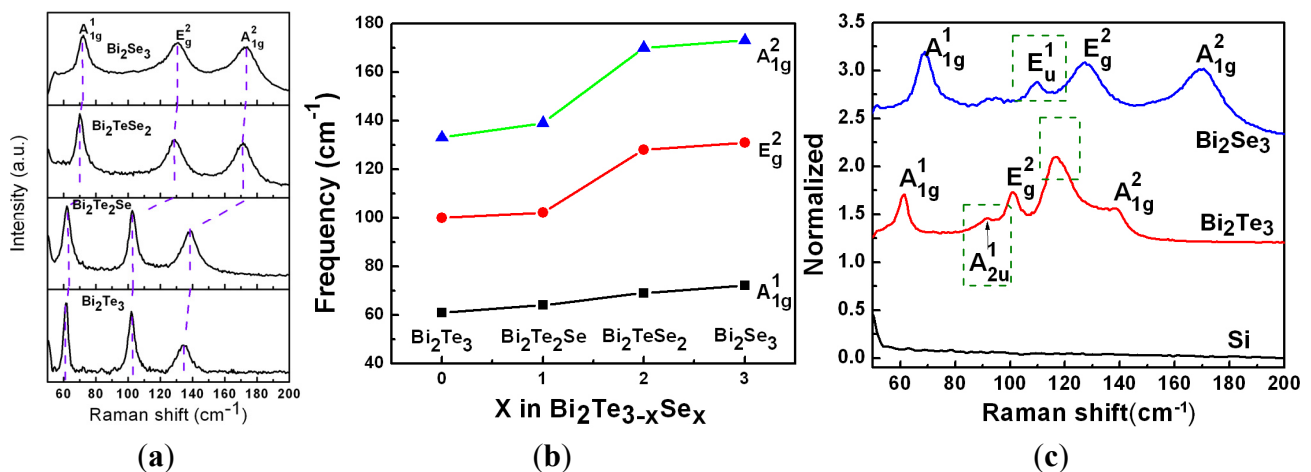

(**c**)　　　　　　　　　(**d**)

Figure 4. Raman spectra of (**a**) Bi_2Te_3, (**b**) Bi_2Te_2Se, (**c**) Bi_2TeSe_2 and (**d**) Bi_2Se_3 measured at four different excitation wavelengths (488 nm (2.54 eV), 514 nm (2.41 eV), 633 nm (1.96 eV), and 785 nm (1.58 eV)).

Figure 5. Raman shift of (**a**) Bi₂Te₃, (**b**) Bi₂Te₂Se, (**c**) Bi₂TeSe₂ and (**d**) Bi₂Se₃ under different excitation wavelengths (488, 514, 633 and 785 nm).

Figure 6. (**a**) Raman spectra of four compounds excited at 785 nm. (**b**) The dependence of Raman peak position on stoichiometric ratio. (**c**) Observation of IR-active vibrational modes in Raman spectra excited at 785 nm. The dashed boxes indicate the peaks of those IR-active modes.

4. Conclusions

In summary, we have demonstrated a practical hydrothermal approach to produce Bi₂Te$_x$Se$_{3-x}$ platelets in a large scale. Material characterizations reveal that these platelets are single crystalline with thickness of 5 nm to 50 nm and size of 400 nm to 5 μm. A systematic Raman spectroscopy study was performed at four visible excitation wavelengths for all four compounds. It is found that the vibrational modes are shifted to higher frequency with more Se in corporation towards the replacement of Te. The characteristic Raman vibrational modes show a weak dependence on laser excitation energy. We observed two IR-active modes in TI crystals, *i.e.*, E$_u$ mode at 110 cm^{-1} for Bi₂Se₃, A$^1_{2u}$ at 92 cm^{-1} for Bi₂Te₃, and the appearance of these modes is mainly due to quantum size effects. The main findings in this work will be beneficial to future electronic, photonic and spintronic applications.

Acknowledgments

Author Contributions

Jian Yuan, Meng Zhao and Qiaoliang Bao conceived the idea for this paper. JianYuan, Wengzhi Yu, Yao Lu, Caiyun Chen and Meng Xu contributed to the experimental processes, measurements, and data analysis. The manuscript was written through contributions of all authors. All authors have given approval to the final version of the manuscript.

Conflicts of Interest

The authors declare no conflict of interest.

References

1. Moore, J.E. The birth of topological insulators. *Nature* **2010**, *464*, 194–198.
2. Fu, L. Topological crystalline insulators. *Phys. Rev. Lett.* **2011**, *106*, doi:10.1103/PhysRevLett. 106.106802.
3. Butler, S.Z.; Hollen, S.M.; Cao, L.; Cui, Y.; Gupta, J.A.; Gutierrez, H.R.; Heinz, T.F.; Hong, S.S.; Huang, J.; Ismach, A.F.; *et al.* Progress, challenges, and opportunities in two-dimensional materials beyond graphene. *ACS Nano* **2013**, *7*, 2898–2926.
4. Zhang, Y.; He, K.; Chang, C.Z.; Song, C.L.; Wang, L.L.; Chen, X.; Jia, J.F.; Fang, Z.; Dai, X.; Shan, W.Y.; *et al.* Crossover of the three-dimensional topological insulator Bi_2Se_3 to the two-dimensional limit. *Nature Phys.* **2010**, *6*, 584–588.
5. Chen, Y.; Analytis, J.; Chu, J.H.; Liu, Z.; Mo, S.K.; Qi, X.L.; Zhang, H.; Lu, D.; Dai, X.; Fang, Z.; *et al.* Experimental realization of a three-dimensional topological insulator, Bi_2Te_3. *Science* **2009**, *325*, 178–181.
6. Zhang, H.; Liu, C.X.; Qi, X.L.; Dai, X.; Fang, Z.; Zhang, S.C. Topological insulators in Bi_2Se_3, Bi_2Te_3 and Sb_2Te_3 with a single Dirac cone on the surface. *Nature Phys.* **2009**, *5*, 438–442.
7. Wang, Z.F.; Su, N.; Liu, F. Prediction of a two-dimensional organic topological insulator. *Nano Lett.* **2013**, *13*, 2842–2845.
8. Qiao, H.; Yuan, J.; Xu, Z.; Chen, C.; Lin, S.; Wang, Y.; Song, J.; Liu, Y.; Khan, Q.; Hoh, H.Y.; Bao, Q.L.; *et al.* Broadband Photodetector Based on Graphene-Bi_2Te_3 Heterostructure. *ACS Nano* **2015**, *9*, 1886–1894.
9. Soni, A.; Yanyuan, Z.; Ligen, Y.; Aik, M.K.K.; Dresselhaus, M.S.; Xiong, Q. Enhanced Thermoelectric Properties of Solution Grown $Bi_2Te_{3-x}Se_x$ Nanoplatelet Composites. *Nano Lett.* **2012**, *12*, 1203–1209.

10. Min, Y.; Moon, G.D.; Kim, B.S.; Lim, B.; Kim, J.S.; Kang, C.Y.; Jeong, U. Quick, controlled synthesis of ultrathin Bi_2Se_3 nanodiscs and nanosheets. *J. Am. Chem. Soc.* **2012**, *134*, 2872–2875.

11. Wang, G.; Zhu, X.G.; Sun, Y.Y.; Li, Y.Y.; Zhang, T.; Wen, J.; Chen, X.; He, K.; Wang, L.L.; Ma, X.C.; *et al.* Topological insulator thin films of Bi_2Te_3 with controlled electronic structure. *Adv. Mater.* **2011**, *23*, 2929–2932.

12. Shi, W.; Yu, J.; Wang, H.; Zhang, H. Hydrothermal synthesis of single-crystalline antimony telluride nanobelts. *J. Am. Chem. Soc.* **2006**, *128*, 16490–16491.

13. Zhang, G.; Wang, W.; Lu, X.; Li, X. Solvothermal synthesis of V–VI binary and ternary hexagonal platelets: The oriented attachment mechanism. *Cryst. Growth Des.* **2008**, *9*, 145–150.

14. Xu, Y.; Ren, Z.; Ren, W.; Cao, G.; Deng, K.; Zhong, Y. Hydrothermal synthesis of single-crystalline Bi_2Te_3 nanoplates. *Mater. Lett.* **2008**, *62*, 4273–4276.

15. Cui, H.; Liu, H.; Li, X.; Wang, J.; Han, F.; Zhang, X.; Boughton, R.I. Synthesis of Bi_2Se_3 thermoelectric nanosheets and nanotubes through hydrothermal co-reduction method. *J. Solid State Chem.* **2004**, *177*, 4001–4006.

16. Mehta, R.J.; Zhang, Y.; Karthik, C.; Singh, B.; Siegel, R.W.; Borca-Tasciuc, T.; Ramanath, G. A new class of doped nanobulk high-figure-of-merit thermoelectrics by scalable bottom-up assembly. *Nature mater.* **2012**, *11*, 233–240.

17. Zhang, J.; Peng, Z.; Soni, A.; Zhao, Y.; Xiong, Y.; Peng, B.; Wang, J.; Dresselhaus, M.S.; Xiong, Q. Raman spectroscopy of few-quintuple layer topological insulator Bi_2Se_3 nanoplatelets. *Nano Lett.* **2011**, *11*, 2407–2414.

18. Song, J.C.; Xia, F.; Zhao, M.; Zhong, Y.L.; Li, W.; Loh, K.P.; Causo, R.A.; Bao, Q.L. Solvothermal growth of bismuth chalcogenide nanoplatelets by the oriented attachment mechanism: An *in situ* PXRD syudy. *Chem. Mater.* **2015**, *27*, 3471–3482.

19. Kong, D.; Dang, W.; Cha, J.J.; Li, H.; Meister, S.; Peng, H.; Liu, Z.; Cui, Y. Few-layer nanoplates of Bi_2Se_3 and Bi_2Te_3 with highly tunable chemical potential. *Nano Lett.* **2010**, *10*, 2245–2250.

20. Richter, W.; Becker, C.R. A Raman and far-infrared investigation of phonons in the rhombohedral V_2–VI_3 compounds Bi_2Te_3, Bi_2Se_3, Sb_2Te_3 and $Bi_2(Te_{1-x}Se_x)_3$ $(0 < x < 1)$,$(Bi_{1-y}Sb_y)_2Te_3$ $(0 < y < 1)$. *Phys. Status solidi* **1977**, *84*, 619–628.

21. Kullmann, W.; Eichhorn, G.; Rauh, H.; Geick, R.; Eckold, G.; Steigenberger, U. Lattice dynamics and phonon dispersion in the narrow gap semiconductor Bi_2Te_3 with sandwich structure. *Phys. Status solidi* **1990**, *162*, 125–140.

22. Zhao, Y.; Luo, X.; Zhang, J.; Wu, J.; Bai, X.; Wang, M.; Jia, J.; Peng, H.; Liu, Z.; Quek, S.Y.; *et al.* Interlayer vibrational modes in few-quintuple-layer Bi_2Te_3 and Bi_2Se_3 two-dimensional crystals: Raman spectroscopy and first-principles studies. *Phys. Rev. B* **2014**, *90*, doi:10.1103/PhysRevB.90.245428.

23. Piscanec, S.; Cantoro, M.; Ferrari, A.; Zapien, J.; Lifshitz, Y.; Lee, S.T.; Hofmann, S.; Robertson, J. Raman spectroscopy of silicon nanowires. *Phys. Rev. B* **2003**, *68*, doi:10.1103/PhysRevB.68.241312.

24. Russo, V.; Bailini, A.; Zamboni, M.; Passoni, M.; Conti, C.; Casari, C.; Li Bassi, A.; Bottani, C.E. Raman spectroscopy of Bi-Te thin films. *J. Raman Spectrosc.* **2008**, *39*, 205–210.

25. Akrap, A.; Tran, M.; Ubaldini, A.; Teyssier, J.; Giannini, E.; Van Der Marel, D.; Lerch, P.; Homes, C.C. Optical properties of Bi_2Te_2Se at ambient and high pressures. *Phys. Rev. B* **2012**, *86*, doi:10.1103/PhysRevB.86.235207.

26. Chis, V.; Sklyadneva, I.Y.; Kokh, K.; Volodin, V.; Tereshchenko, O.; Chulkov, E. Vibrations in binary and ternary topological insulators: First-principles calculations and Raman spectroscopy measurements. *Phys. Rev. B* **2012**, *86*, doi:10.1103/PhysRevB.86.174304.

27. Saito, R.; Jorio, A.; Souza Filho, A.; Dresselhaus, G.; Dresselhaus, M.; Pimenta, M. Probing phonon dispersion relations of graphite by double resonance Raman scattering. *Phys. Rev. Lett.* **2001**, *88*, doi:10.1103/PhysRevLett.88.027401.

28. Irfan, B.; Sahoo, S.; Gaur, A.P.; Ahmadi, M.; Guinel, M.J.F.; Katiyar, R.S.; Chatterjee, R. Temperature dependent Raman scattering studies of three dimensional topological insulators Bi_2Se_3. *J. Appl. Phys.* **2014**, *115*, doi:10.1063/1.4871860.

29. Han, X.; Tao, H.; Gong, L.; Wang, X.; Zhao, X.; Yue, Y. Origin of the frequency shift of Raman scattering in chalcogenide glasses. *J. Non-Cryst. Solids* **2014**, *391*, 117–119.

30. Wang, C.; Zhu, X.; Nilsson, L.; Wen, J.; Wang, G.; Shan, X.; Zhang, Q.; Zhang, S.; Jia, J.; Xue, Q. In situ Raman spectroscopy of topological insulator Bi_2Te_3 films with varying thickness. *Nano Res.* **2013**, *6*, 688–692.

31. Pine, A.S.; Dresselhaus, G. Raman spectra and lattice dynamics of tellurium. *Phys. Rev. B* **1971**, *4*, 356.

32. Zhang, Q.; Zhang, J.; Utama, M.I.B.; Peng, B.; De la Mata, M.; Arbiol, J.; Xiong, Q. Exciton-phonon coupling in individual ZnTe nanorods studied by resonant Raman spectroscopy. *Phys. Rev. B* **2012**, *85*, doi:10.1103/PhysRevB.85.085418.